Stellar occultations observed by SPICAM on Mars Express

Eric Quémerais,[1] Jean-Loup Bertaux,[1] Oleg Korablev,[2] Emmanuel Dimarellis,[1] Charles Cot,[1] Bill R. Sandel,[3] and Didier Fussen[4]

Received 7 October 2005; revised 3 February 2006; accepted 28 March 2006; published 7 September 2006.

[1] Spectroscopy for the Investigation of the Characteristics of the Atmosphere of Mars (SPICAM) is the first instrument orbiting a planet other than Earth that is dedicated to the technique of stellar occultation. During the first year of operation on board Mars Express, SPICAM observed more than 500 star occultations, yielding vertical profiles of CO_2, ozone, and dust/clouds/aerosols. We review the principles of a star occultation in the absorptive regime, emphasizing two advantages of this method: an absolute value is obtained from a relative measurement without the need for an absolute calibration of the instrument, and the altitude of the measurement is accurately known because it depends only on the position of the spacecraft and not on the pointing of the instrument. We describe a general algorithm used for all occultations. First, we derive from the raw data the transmission of the atmosphere as a function of wavelength, $T(\lambda, z)$, taking account of instrument-specific factors. Then a spectral inversion retrieves the slant densities (local densities integrated along the line of sight) of all absorbing species for each measurement of the transmission $T(\lambda, z)$ during the occultation. Finally, a vertical inversion retrieves the vertical distribution of the local densities from the series of the slant density measurements. This vertical inversion includes a new scheme of Tikhonov regularization. This paper will serve as a reference for the SPICAM Mars Express data which will be systematically made available to the public in the PDS-like archive managed by ESA.

Citation: Quémerais, E., J.-L. Bertaux, O. Korablev, E. Dimarellis, C. Cot, B. R. Sandel, and D. Fussen (2006), Stellar occultations observed by SPICAM on Mars Express, *J. Geophys. Res.*, *111*, E09S04, doi:10.1029/2005JE002604.

1. Introduction

[2] The use of the stellar occultation technique in space has been reviewed by *Smith and Hunten* [1990]. It was first discussed in detail by *Hays and Roble* [1968] in a seminal paper, and used to measure terrestrial ozone with the astronomical satellites OAO-2 and Copernicus (OAO-3). With OAO-2 in 1970 and 1971, *Hays et al.* [1972] and *Hays and Roble* [1973] detected directly for the first time the mesospheric ozone maximum by absorption of starlight in the UV. The maximum had been previously inferred by *Evans et al.* [1970] from rocket sounding of the O_2 ($^1\Delta$) (1.27 m) and O_2 ($^1\Delta$) (760 nm) airglow emissions, which are produced by photo-dissociation of ozone. In 1975 and 1976, the third Orbiting Astronomical Observatory (OAO-3, soon renamed Copernicus) was also used to measure terrestrial ozone above 45 km from UV absorption in a wavelength region similar to that of the OAO-2 measurement [*Riegler et al.*, 1976, 1977].

[3] All these early stellar occultations measurements suffered because only one wavelength was monitored, opening the possibility for confusion in the identity of the absorbing species. The advent of CCDs and other multi-pixel detectors, measuring the entire transmission spectrum at once, dramatically increased the capability of stellar occultation compared to using filters or scanning spectrometers. The first multi-pixel occultation measurement (to our knowledge) was inaugurated with the Voyager 1 and 2 ultraviolet spectrometers (UVS). In 1979, an occultation of the star α Leonis by the atmosphere of Jupiter was observed from a distance of 14 million km by Voyager 1 in the full range 90–170 nm, thereby probing the vertical profiles of H_2 and methane [*Festou et al.*, 1981]. Since then, this technique has been fostered at Service d'Aéronomie, in particular for the study of the atmosphere of Mars with the SPICAM instrument. A first instrument dedicated to multi-wavelength stellar occultations was destroyed in November 1996 by the launch failure of the Russian mission Mars 96. Now a smaller version, SPICAM Light, the subject of this paper, is flying on ESA's Mars Express mission.

[4] The concept of the multi-wavelength stellar occultation has also been proved using the U.S. military spacecraft Midcourse Space Experiment (MSX), where the UVISI instrument (Ultraviolet and Visible Imagers and Spectrometers) has already provided very interesting results using this technique [*Yee et al.*, 2002]. However, the UVISI was not specially designed for this task. GOMOS (Global Ozone Monitoring by Occultation of Stars) is the first space instrument specially designed and dedicated to the study

[1] Service d'Aéronomie, Verrières le Buisson, France.
[2] Space Research Institute (IKI), Moscow, Russia.
[3] Lunar and Planetary Laboratory, Tucson, Arizona, USA.
[4] Institut d'Aéronomie Spatiale, Brussels, Belgium.

Copyright 2006 by the American Geophysical Union.
0148-0227/06/2005JE002604

of the atmosphere of Earth by the technique of stellar occultations. GOMOS was launched successfully in 2002 on board the ENVISAT mission from the European Space Agency (ESA), one of nine Earth Observations instruments. One of the three instruments devoted to atmospheric chemistry, GOMOS is charged with establishing the 3-D distribution of ozone in the stratosphere and monitoring its trend as a function of altitude, taking advantage of the particularly high absolute accuracy offered by the stellar occultation technique.

[5] While observing a stellar occultation with UVISI on MSX required orienting the entire 6-ton spacecraft to the star, GOMOS has a moving mirror that directs the field of view to the occultation target, without perturbing the other Earth Observations instruments on ENVISAT, which are nadir oriented. On the Mars 96 Russian mission, the spacecraft was to be oriented to the sun, and a dedicated 40 kg platform pointed SPICAM toward the star with active pointing control. On Mars Express (MEX), we took advantage of the pointing capabilities of the whole spacecraft, and the instrument is mounted with its viewing axis fixed parallel to those of the other optical instruments. To observe an occultation of a star, the whole spacecraft is oriented (as with MSX) toward the selected star without active pointing. Cassini's Ultraviolet Imaging Spectrograph Investigation (UVIS) works similarly [*Esposito et al.*, 2005].

[6] After the demise of Mars 96, when ESA offered the possibility of reflying some Mars 96 instruments on MEX through a competitive Announcement of Opportunity in 1999, the SPICAM team felt that the concept of the original instrument had to be modified substantially for lower mass, which was much more limited on MEX. By simulating stellar occultations, *Korablev et al.* [2001] demonstrated that a modest 16 cm^2 aperture telescope and a simple combination of a parabolic off-axis telescope and concave grating, would give accurate CO_2, ozone, and dust retrievals for the 40 brightest UV stars in the range 110–310 nm. Therefore a new version (SPICAM Light) was proposed for MEX and accepted at a mass of 4.8 kg (instead of 17 kg on Mars 96).

[7] Below we describe the general principles of the stellar occultation method, with particular emphasis on the case of SPICAM Light on MEX (simply SPICAM henceforth). See also *Bertaux et al.* [2005] for an illustration. To begin the measurement, the spacecraft is commanded to point its +Z axis (the optical axis of all optical instruments, within alignment errors) to a selected star, at a certain point along the orbit. When the star is high above the horizon, SPICAM records the spectrum of the star $S_0(\lambda)$ unattenuated by atmospheric absorption. A few seconds later, the spectrum of the same star seen through the atmosphere (just above the horizon) is again recorded. This spectrum $S(\lambda, z)$ is modified by the absorption of all atmospheric constituents integrated over the line of sight from MEX to the star, according to the Beer-Lambert law,

$$S(\lambda, z) = S_0(\lambda)\, \exp(-\sigma_\lambda N(z)), \tag{1}$$

where λ is the wavelength, z is the minimum altitude of the line of sight above the horizon (also called the tangent height, or tangent altitude), $N(z)$ (mol.cm^{-2}) is the integrated quantity of CO_2 along the line of sight (slant density) and σ_λ the absorption cross section of CO_2. Here, only CO_2 absorption is considered for clarity. Therefore SPICAM has measured the atmospheric spectral transmission $T(\lambda, z) = S(\lambda, z)/S_0(\lambda)$ at altitude z. Determining this transmission from raw telemetry data, taking into account several instrumental factors, is called the Level 1B processing, and is described in section 2.

[8] From equation (1), one derives

$$N(z) = -\frac{1}{\sigma_\lambda} \log \frac{S(\lambda, z)}{S_0(\lambda)}. \tag{2}$$

Then, during a single occultation, a series of tangential column (slant) densities $N(z_j)$ are obtained at various altitudes z_j. This series can be inverted (vertical inversion) to yield the vertical distribution of the local density $n(z)$ of CO_2 (mol.cm^{-3}), assuming that the atmosphere is locally spherically symmetric. This vertical inversion is (in principle) straightforward with the so-called onion-peeling technique. We will show later that some care must be taken during the vertical inversion, in order to avoid strong spurious oscillations in the vertical profile $n(z)$.

[9] Besides the extreme simplicity of the retrieval algorithm when compared to other methods, the occultation technique has an enormous advantage readily apparent in equation (2): an absolute estimate of $N(z)$ is obtained from the ratio of two measurements taken a few seconds apart with the same instrument. The method is inherently self-calibrated, and even if the spectral sensitivity of the instrument has long-term drifts, the ratio will be measured correctly and hence also the slant density $N(z)$ (density integrated along the Line of Sight LOS). This immunity to long-term drift is of course ideal for the study of seasonal and interannual variations of CO_2, ozone and other constituents. SPICAM's fundamental measurement is this ratio, which is the spectral transmission of the atmosphere as a function of the tangent height of the line of sight.

[10] In principle, one could use a detector for only one wavelength λ, if CO_2 were the only absorbing species at this wavelength. This is not the case in the UV range of SPICAM, as shown in Figure 5, which displays the cross sections of CO_2 and ozone with an additional contribution of dust. Therefore, in order to properly identify each of the atmospheric absorbers separately, one has to measure in a wide wavelength domain with a sufficient spectral resolution. For several species, equation (1) becomes

$$T(\lambda, z) = \frac{S(\lambda, z)}{S_0(\lambda)} = \exp(-\Sigma_i \sigma_i N_i(z)). \tag{3}$$

Therefore, before the vertical inversion the first step of the Level 2 processing is to retrieve each quantity $N_i(z)$ for each measured altitude; this is the so-called spectral inversion, or separation of constituents. One needs to measure at least as many different wavelengths as the number of constituents. In the case of SPICAM, a CsTe cathode was selected for the Hamamatsu image intensifier UV detector, providing a useful sensitivity in the wavelength range 110–310 nm, but still *solar blind* (insensitive to visible light). After the spectral inversion, a vertical inversion is performed separately for each constituent. Within the spectral range of SPICAM, CO_2, O_3, possibly O_2 [*Korablev et al.*, 2001], and aerosols may be measured as a function of altitude. Except for aerosols, these absorbers have well-defined

absorption spectral signatures, which permits disentangling each of them from the combined spectrum of the atmospheric transmission.

[11] Another important feature of stellar occultations is that the altitude of the measurement is entirely defined by the direction to the star and the position of the spacecraft. The atmosphere of Mars is rather thin, and refraction of the starlight can be neglected. The data are free of the scintillations observed in Earth's atmosphere by, e.g., GOMOS. The MEX position is known with an accuracy better than ±0.5 km, ensuring the same accuracy on the knowledge of z. Unlike techniques based on measuring limb emissions, the altitude of the measurement does not depend on the attitude of the spacecraft and instrument. The vertical resolution is determined by the integration time, the sampling rate, and the vertical velocity of the tangent point, which for SPICAM are 0.64 s, 1 Hz and a few km/s (depending on the geometry), resulting in a typical vertical resolution of a few kilometers at most.

[12] SPICAM can also observe solar occultations by using a side-looking port [*Bertaux et al.*, 2005]. The solar occultation technique shares with stellar occultations the advantage that an absolute quantity is derived from relative measurements. Using stars instead of the sun has some additional advantages:

[13] 1. The spectrum of the sun is somewhat weak below 200 nm, making CO_2 absorption more difficult to measure, while hot UV stars have a reasonably constant signal over the whole range of interest.

[14] 2. Knowledge of the measurement's altitude is excellent (±0.5 km) because the star is a point source, but the solar disk is an extended, nonuniform source, so the pointing of the instrument must be known accurately, and preferably the same portion of the sun must always be observed during the occultation.

[15] 3. Solar occultations occur only at dawn or dusk, when the photochemistry regime of the atmosphere is changing rapidly with a strong diurnal variation of ozone (even along the LOS), while the LOS to a star usually pertains to a well defined regime (day or night).

[16] 4. From the orbit of MEX, there are only two solar occultation opportunities per orbit, offering coverage of a limited range of latitudes, while stars allow observing a larger latitude range. Even for stellar occultations, the latitude range is somewhat restricted, because the SPICAM stars are not distributed uniformly on the sky, but concentrated along the galactic plane, or rather the Gould Belt.

[17] 5. Because the sun is an extended source, and a certain portion of the solar disk is encompassed by the FOV for each measurement, the vertical resolution is defined by the projection at the limb of the instantaneous FOV. This changes with the distance to the limb, which may be up to 10,000 km for the MEX orbit.

[18] There are some drawbacks to using stars: (1) they are weak sources, providing a lower S/N ratio, (2) they have different brightnesses and spectra and hence different uncertainties, and (3) night side measurements are preferred, because on the day side, emissions from the bright limb compete with the stellar flux. Nevertheless, the inherent advantages of the stellar occultation method overcome these drawbacks, and a certain priority was attached to stellar occultations when programming SPICAM observations.

[19] This paper presents some stellar occultations by the atmosphere of Mars and the methods to derive density profiles of carbon dioxide, ozone and aerosols below 150 km altitude. The UV channel of SPICAM has recorded hundreds of stellar occultations. These observations were mainly performed on the nightside of the planet to avoid contamination of the spectra by sunlight reflected from the surface of Mars or from dust clouds.

[20] The UV channel of SPICAM has a pass-band between 110 nm and 310 nm. It is a full UV imaging spectrometer that spatially resolves 288 spectra along its slit. This slit is placed at the focus of a off-axis parabolic entrance mirror. During a star occultation, the slit is retracted from the light path; then large pointing errors are tolerable, since the total FOV is in this case about $1^\circ \times 3^\circ$. Behind the focal plane, a holographic grating spreads the spectrum of any point of the focal plane on the CsTe photocathode of the intensified CCD detector. If the star is the only object in the FOV, only its spectrum will be recorded on the detector, with an image quality which depends on the position in the FOV, providing at its best a spectral resolution of roughly 1.5 nm (about 3 pixels). Any emissions from the limb or disk of Mars will appear also above and below the star spectrum, providing the possibility to subtract them, if they are not too intense.

[21] For each line of the CCD, the spectrum is spread over 384 pixels. Although 288 spectra are spatially resolved, only 5 are transmitted to Earth, owing to a limitation on telemetry. To increase the signal to noise ratio, the five transmitted spectra are the sum of a chosen number of physical lines of the CCD. In most cases, this number is 8. The central band of 8 lines contains most of the star signal (90%), while the other bands contain the rest of the signal. This spread over more than one band is due to the spatial dispersion of the star signal by the grating (vertical axis of CCD). The misalignment of SPICAM's FOV with the spacecraft axis was actually determined from star observations outside the atmosphere. One pixel of the CCD corresponds to 0.01° at the focal plane. It was found that the absolute pointing accuracy of MEX is better than 0.01°, and the stability is excellent. Therefore we have attempted some star occultations on the day side, with the slit in place, to decrease the contribution of the bright limb. These observations, allowing measurements down to 50 km altitude, will be reported elsewhere.

[22] In the next paragraph, we present the scheme that we have developed to derive density profiles from the SPICAM UV occultation data. First, we show how data are used to compute transmission through the atmosphere as a function of altitude. From the transmission, we show how slant densities of carbon dioxide and ozone are computed. This step is called spectral inversion. Finally, we compute local density profiles assuming a spherically symmetric atmosphere at the point of occultation. This is called vertical inversion. For each step we give special attention to computing the uncertainties in the retrieved values. The last part shows how temperature profiles can be derived assuming hydrostatic equilibrium.

[23] Three companion papers present the scientific significance of the atmospheric parameters retrieved with the algorithm described here. Dust/aerosols/clouds are presented by *Montmessin et al.* [2006], while ozone vertical

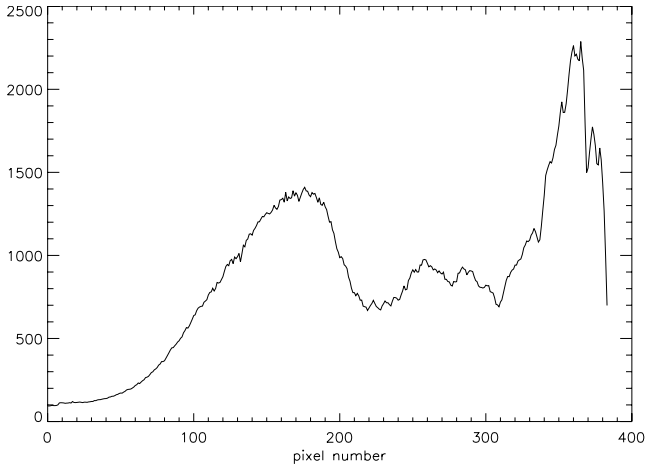

Figure 1. Mean spectrum for a stellar observation outside the atmosphere of Mars. This spectrum is the average of 52 individual spectra. The Mars Nearest Point for each line of sight is more than 200 km from the surface. No correction for instrumental effects has been applied. The x axis gives the pixel number, and the y axis is in units of raw counts. Longer wavelengths are toward the left. The star is θ Carinae (HR 4199).

distributions are compared with chemistry models by *Lebonnois et al.* [2006]. CO_2 density profiles and temperature profiles are presented and compared to a GCM model by F. Forget et al. (manuscript in preparation, 2006).

2. SPICAM Occultation Data and Transmission Computation

2.1. Data Presentation

[24] The SPICAM instrument is described by *Bertaux et al.* [2005], who show a schematic diagram. The SPICAM detector is an intensified CCD, an image intensifier coupled to a CCD through stacks of fiber optics. The Hamamatsu image intensifier has a CsTe photocathode deposited on a MgF_2 window. Photo-electrons created at the photocathode by UV photons are accelerated by the high voltage applied to a microchannel plate, creating a cloud of electrons that is again accelerated to a phosphor screen. The resulting pulse of green light is transmitted through the fiber optics to the CCD pixels. The charge on each pixel is read and digitized to 12 bits, giving a maximum of 4095 ADU (Analog to Digital units). Therefore the detector is used in a pseudo-counting mode [*Sandel and Broadfoot*, 1986]. The gain of the MCP may be adjusted so that a single photo-electron created at the cathode will produce 1 to 40 ADUs in the CCD, spread over ≈6 pixels on the CCD matrix.

[25] The CCD is an array of 408 by 288 pixels. The 288 lines are perpendicular to the slit axis and parallel to the dispersion plane of the grating. The spectra are spread along the lines of the CCD. Of the 408 pixels in each line, 384 are used to measure the spectra. The remaining pixels, some of which are masked, are used to determine the dark current of the CCD.

[26] Each measurement has an integration time of a few hundred milliseconds. A typical value is 640 ms. The gain of the MCP is adjusted according to the brightness of the source. Due to limited telemetry bandwidth, only 5 bands of 408 pixels are transmitted to Earth. The 5 bands are formed by summing individual lines by 1, 2, 4, 8, 16 or 32. Typically, for stellar occultations, each band is the sum of 8 or 16 physical lines of the CCD. Most of the stellar signal is included in the central band.

[27] A typical occultation lasts a few minutes. During the entire observation, the line of sight is pointed toward a chosen star with a suitable emission spectrum in the range 100–310 nm. The stellar spectrum is measured for a few minutes outside of the atmosphere of Mars. These data are used to compute the reference spectrum $S_o(\lambda)$. Then, as the spacecraft travels along its orbit around Mars, the star moves behind the planet and the line of sight approaches the surface of Mars. SPICAM records a spectrum every second, which corresponds to 1 to 3 km in altitude depending on the geometry of observation. Half of the SPICAM occultation observations are de-occultations, i.e., the star is rising above the limb of Mars instead of setting.

[28] Figure 1 shows a typical reference spectrum recorded by SPICAM before an occultation. The spectrum is shown in pixel number because wavelengths have not yet been assigned at this step in the processing. This is because the slit is removed during occultations, so the stellar spectrum appears on the CCD at a position that depends on the position of the star within the field of view. For some occultations, the spectrum is shifted by up to tens of nanometers because the star was far from the center of the field. The next paragraph shows how wavelengths are assigned. We note that during an occultation the spacecraft pointing stability is very good, so the spectrum is stationary on the CCD. Therefore a single mapping of pixel to wavelength is appropriate for an entire occultation observation.

[29] In the case of 5 bands of 16 lines, we have been able to measure the spread of the stellar spectrum across the dispersion plane of the grating, i.e., in the spatial dimension perpendicular to the spectral dimension. Numbering the bands of 16 lines from 0 to 4 from bottom to top, and with a star centered on the middle band (band number 2), we find the following fractions shown in Table 1.

[30] Ideally, only the middle band should be used in the data processing because adding an additional band of data also adds the noise of the dark current of that band. However, information from other bands is useful to characterize any limb emission which could be superimposed on the starlight.

2.2. Dark Current

[31] The Thomson TH7863 CCD used in the UV channel of SPICAM has an average dark current (DC) of about 10–20 ADU per second. Moreover to avoid bias in the statistics of low signals, an offset of roughly 20–30 ADU is applied to the data before digitization. This amounts to a total of roughly 40 ADU which must be removed. This number is not constant in time, because it increases with the temperature of the CCD. It is also not uniform from

Table 1. Vertical Spread of Stellar Flux

Band 0 (Bottom)	Band 1	Band 2 (Center)	Band 3	Band 4 (Top)
0.010	0.028	0.902	0.047	0.013

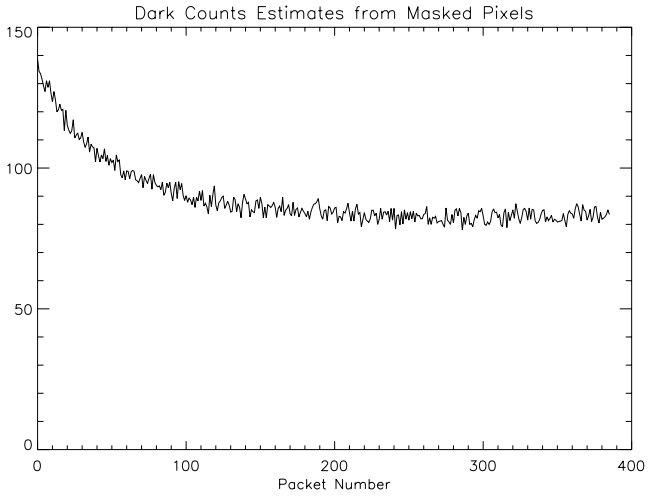

Figure 2. Variation of the dark current indicator DCI as a function of time. There is one value per second, i.e., the x axis is also in seconds since the beginning of the observation. The DCI value is obtained by averaging the count rates in the masked pixels. The fast decrease at the beginning is the effect of the Peltier cooler which decreases the temperature of the detector.

pixel to pixel over the CCD. We will refer to the pattern of variation of the dark current over the CCD as the dark current non-uniformity (DCNU). Fortunately, the DCNU is very stable and can be determined by pointing the instrument toward a dark target such as the night side of Mars.

[32] Of the 408 pixels in a line of the CCD, 384 are used to measure the spectrum. Some of the remaining pixels on one side are physically masked from light. They are used to determine the sum of the offset and the dark current. Figure 2 shows the variation of the average of the counts for the masked pixels (called the Dark Current Indicator (DCI)), as a function of time. This variation depends on the temperature of the detector. In this case, a Peltier cooler inside the detector keeps the temperature roughly constant, except for the fast decrease at the beginning of the observation. For some observations, the Peltier cooler was not activated. In those cases, we saw an almost linear increase of the dark current as a function of time. The Dark Current Indicator is used to evaluate the temporal variation of the DC but it is not equal to the DC. Observations made on the night side of Mars, where all counts are dark current, show a clear linear relation between the mean dark current and the DCI. However, the average dark current is roughly 15% higher than the DCI (here offset counts are included in the total dark current). The reason for this is not clear.

[33] We describe one way to remove the dark current that can be applied if the line of sight crosses the nightside of Mars at some point of the observation, either after the star occultation or before the star rises above the limb. First we determine the DCI as a function of time during the whole observation. Then we use the Mars dark surface observations to find the linear relation between the mean dark current and the DCI. We can then subtract from each pixel the corresponding mean DC multiplied by its DCNU coefficient. The DCNU coefficient (see Figure 3) is found by averaging the spectra obtained on the night side of Mars. In that case, only the middle band is used. Figure 3 shows a typical result of this processing. The top line shows the sum of the counts of the 384 pixels in the middle band as a function of time. The top thick line is uncorrected for dark current, and the bottom line has been corrected.

[34] The previous scheme cannot be applied unless the nightside of Mars is observed at some time during the observation. An alternate scheme uses bands 1 and 3 to determine the DC of band 2. We compute the DCI for bands 1, 2 and 3 and find the proportionality coefficients between them. Then we remove the DC determined from bands 1 and 3 from the middle band. This method has several disadvantages. First, the DCNU effect is neglected because only one value is determined for all pixels. Second, we add the noise of the dark current of bands 1 and 3 to our transmission values. Finally, as pointed out above, a fraction of the signal of the star is spread over bands 1 and 3 (3% and 5%, respectively). This means that the reference spectrum must be computed in the same way or we will bias the computation of the transmission.

[35] The transmission is computed by dividing each dark-current-corrected spectrum by the reference spectrum obtained outside the atmosphere of Mars. For each spectrum, we also compute from orbital files the distance of the LOS to the center of Mars. We then subtract the radius of an ellipsoid representing a standard Mars equipotential (variable with latitude), to find the altitude of the LOS, or of the Mars Nearest Point (MNP) of the LOS. Therefore this altitude is unrelated to the actual relief of Mars, but it is the relevant quantity for atmospheric measurements and comparisons with models.

[36] Figure 4 shows examples of stellar spectra obtained in this way during one occultation.

[37] In the next section we show how a wavelength is assigned to each pixel, taking into account the displacement

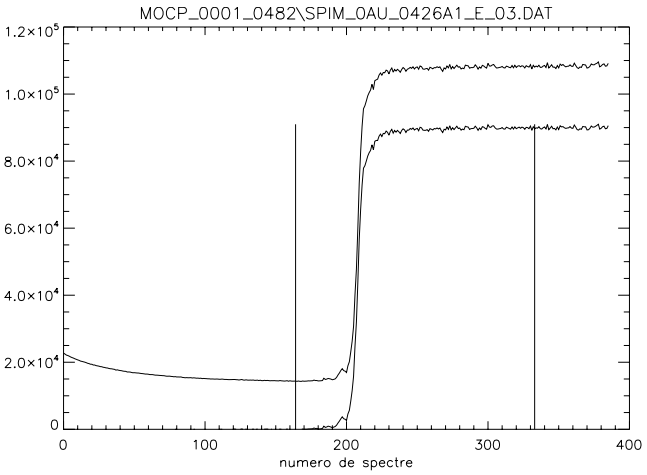

Figure 3. Sum of the spectra between pixels 30 and 180 as a function of spectrum number or seconds since the beginning of the observation. The thick upper line shows the uncorrected data. The thinner line shows the sum obtained for corrected spectra. The left vertical line marks zero altitude, and the right vertical line shows 200 km altitude. Below zero altitude, i.e., when the star is behind the planet, the sum for the corrected spectra is equal to zero as expected.

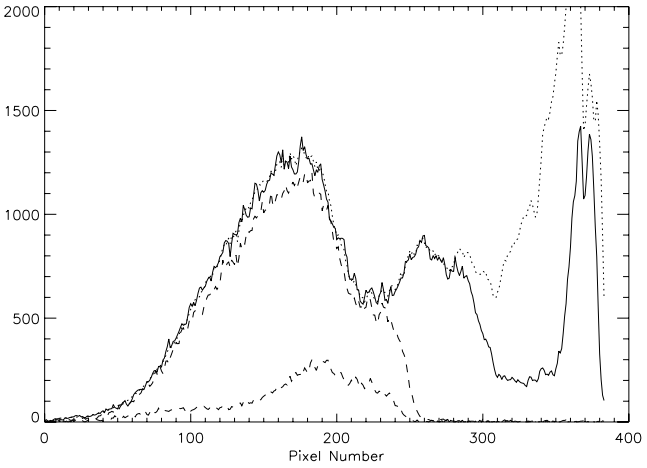

Figure 4. Spectra of the same star recorded at different altitudes above Mars. These spectra have been corrected for instrumental effects. The x axis shows pixel number, and the y axis is in ADU unit. Longer wavelengths are toward the left. The dotted line shows the mean reference spectrum outside the atmosphere (above 200 km here). The dashed and solid lines show spectra recorded for a LOS going through the atmosphere. The solid line shows a spectrum where CO_2 absorption is not saturated. The dashed lines show spectra with saturated CO_2 absorption.

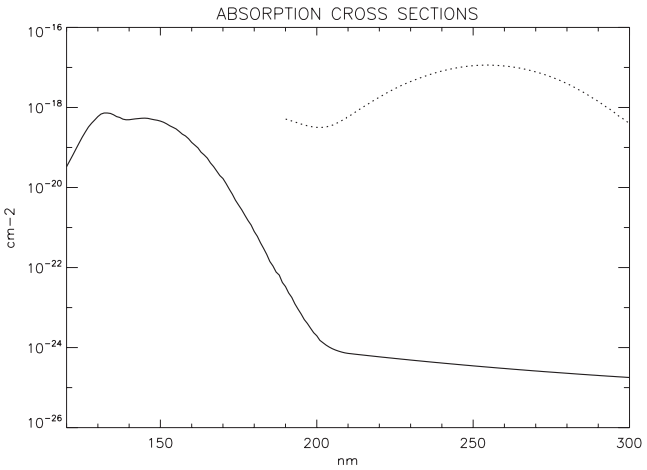

Figure 5. Absorption cross sections of CO_2 (thick line) and O_3 (dotted line) used in the inversion [from *Yoshino et al.*, 1996]. In the inversion we have assumed that the cross sections do not depend on temperature. The values shown here correspond to a temperature of 195 K. Cross-section values are averaged on a 1-nm interval to account for the spectrometer resolution. A sliding mean over 3 pixels has also been performed to account for the point spread function of the spectrometer. In the case of CO_2, Rayleigh scattering extinction is added and becomes important above 210 nm.

in wavelength that may arise because the star is not centered in the field of view.

3. Spectral Inversion

3.1. Cross Sections

[38] To perform the spectral inversion, i.e., to determine the slant densities of the absorbing species, we must know their absorption cross sections. In the SPICAM UV transmission spectra, we see three different absorption signatures.

[39] First, below 150 km altitude there is a clear signature of CO_2 absorption below 200 nm. Also below 50 km, we often see ozone absorption centered around 250 nm. Figure 5 gives the empirical cross sections used in the spectral inversion algorithm. The CO_2 cross sections are from *Yoshino et al.* [1996]. The fine structure oscillations are averaged over 1 nm to account for the pixel size of SPICAM and the 1.5 nm width of the point spread function. As mentioned above, maxima in the CO_2 and O_3 cross sections are clearly separated, with CO_2 absorbing below 200 nm and ozone centered around 250 nm.

[40] Wavelengths are assigned by examining data for which the maximum CO_2 absorption is unsaturated. Figure 6 shows two examples of such cases above 100 km. For these spectra, ozone and aerosol absorption are absent. Then, we can determine the wavelength shift by fitting these transmission spectra with models including the cross section shown in Figure 5. This is repeated for all the spectra with unsaturated CO_2 absorption, usually 5 or 6 per occultation, thus yielding a very accurate wavelength assignment.

[41] The third absorption feature in the SPICAM transmission data is due to aerosols or dust in the atmosphere. The spectral dependence of this absorption is less characteristic than for CO_2 and ozone. In our forward model of the transmission, we take the wavelength dependence of the cross section to be proportional to $1/\lambda^{\alpha}$, where the angström exponent α is close to 1 and increases for smaller particles.

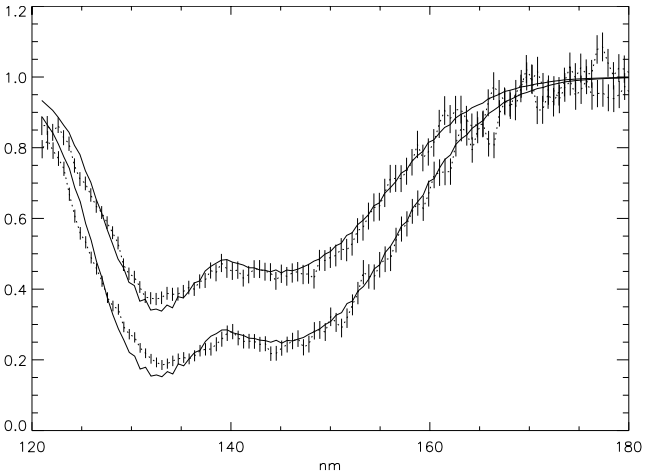

Figure 6. Typical transmission spectra above 100 km used to perform the wavelength assignment. Transmissions for 2 altitudes are plotted. The data (dotted line) are shown with statistical errors. The solid lines show the modeled transmission. Because the star is not always at the center of the field of view, we need to determine the possible shift of the observed spectra on the CCD. This is done by fitting the data with models using the CO_2 cross section shown in Figure 5, because only CO_2 has a significant absorption above 100 km altitude. We allow for an unknown shift on the x axis and determine its value in the fit. This is a sensitive indicator because of the small bumps in transmission around 140 nm.

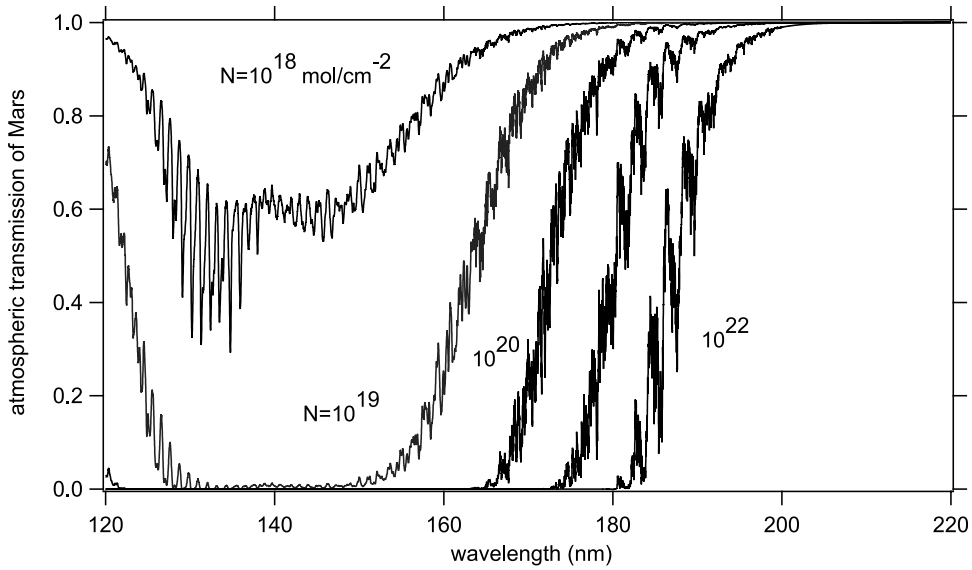

Figure 7. Variation of the spectral transmission of pure CO_2 as a function of the slant density (in mol.cm^{-2} along the LOS). This forward model is computed for the CO_2 cross section of *Yoshino et al.* [1996] at 195 K, taken at high spectral resolution. The large variation of the CO_2 cross section in the UV allows probing a large range of altitude (≈40 to 150 km) in the atmosphere of Mars. The high spectral resolution variations are smoothed out by the ≈1.5 nm spectral resolution of SPICAM.

When the fit is performed, we can choose to fix the value of α or to let it vary with altitude.

3.2. Retrieval of Slant Densities

[42] Slant densities are computed using the cross sections described above. The measured transmission at each altitude is fit by a forward model of the transmission as described in equation (3). Examples of this forward model are shown in Figure 7, but computed at the high spectral resolution available from CO_2 cross section of *Yoshino et al.* [1996]. The algorithm computes the transmission for an averaged cross section, matched to the spectral resolution of SPICAM, in order to save computing time. One transmission spectrum consists of about 300 independent measurements, and only 4 parameters need be derived: CO_2 and ozone slant densities, and the dust optical thickness and angström coefficient α. The best fit values of these parameters are found by minimizing the sum (over all pixels) of squares of differences between the measured transmission and the forward model transmission (weighted by the inverse of square of errors for each pixel). The best-fit solution is found through a Levenberg-Marquardt fitting algorithm described by *Press et al.* [1986].

[43] Figure 8 shows three examples of results obtained with this method. The lower curve corresponds to a transmission profile close to the planet (about 10 km). Aerosol absorption is very strong (maximum transmission below 0.1), but carbon dioxide and ozone absorption features are still clearly visible. The middle curve corresponds to a profile recorded around 40 km altitude. In that case the maximum transmission is around 0.25. The top curve shows a profile with small absorption features of ozone and aerosols. Above 100 km, most of the profiles show only carbon dioxide absorption features.

3.3. Vertical Profiles of Slant Densities

[44] Figure 9 shows a typical result of a vertical profile of slant CO_2 densities obtained after the spectral inversion of a stellar occultation data set. The slant density is the integral of the local density over the line of sight. It is shown in units of cm^{-2}. The slant density multiplied by the cross section is equal to the total optical thickness if the cross section is assumed independent of temperature.

[45] This figure shows that the slant density is very well defined between 40 and 140 km. At altitudes above 140 km, the transmission is very close to unity and detection is

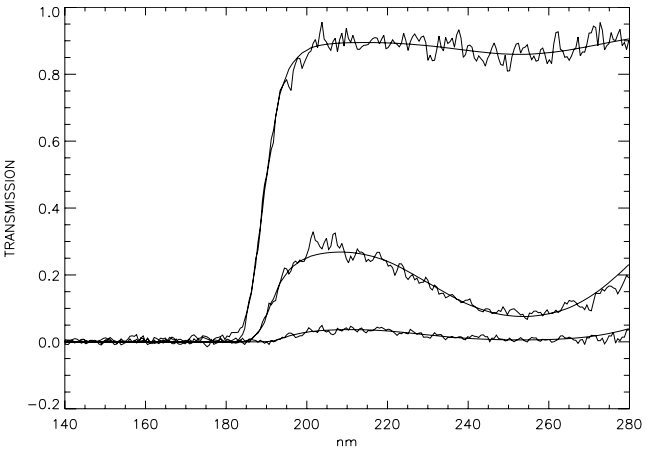

Figure 8. Three examples of transmission profiles and corresponding fit results obtained with a Levenberg-Marquardt fit algorithm. The CO_2 absorption is dominant below 190 nm. The corresponding altitudes are around 10 km, 30 km, and 50 km. Ozone absorption is seen for all these altitudes in that particular case.

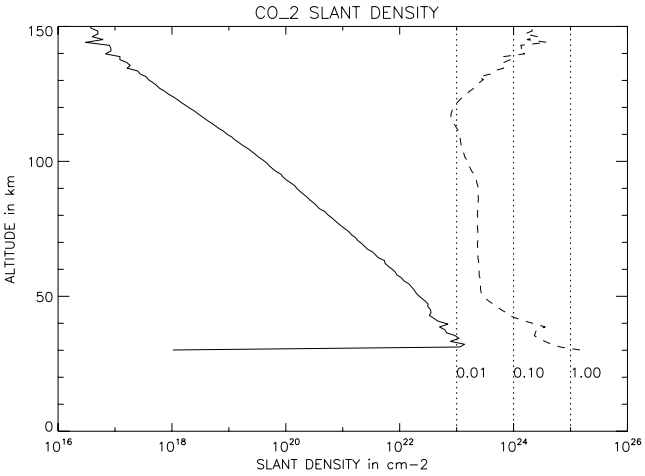

Figure 9. Vertical profile of CO_2 slant density in cm^{-2} obtained from one occultation. This is obtained by assuming that the absorption cross section of CO_2 is independent of temperature. Relative error bars resulting from the Levenberg-Marquardt algorithm are displayed on the right-hand panel. They are very small in the range 45–130 km, covering a dynamic range of 10^5 in slant density of CO_2. This is possible because of the huge variation of CO_2 cross section in the wavelength range 130–200 nm covered by SPICAM.

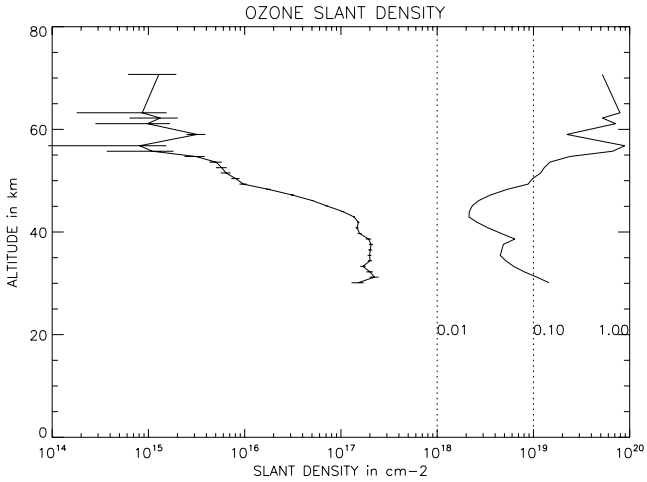

Figure 10. Vertical profile of ozone slant density in cm^{-2} obtained from the same occultation as in the previous figure. Here ozone absorption becomes marginal above 45 km. At lower altitudes the accuracy is limited by the amount of aerosols in the atmosphere. Relative uncertainties are shown on the right-hand panel. They range between 0.01 and 1.00.

limited by the signal to noise ratio. Above 150 km, results are dominated by noise and are not used in the next step, the vertical inversion. Below 40 km, the transmission is mainly affected by aerosol extinction. In that altitude range, the CO_2 absorption profile can be masked by dust and aerosols. A few profiles obtained above very cold areas of the planet show a much clearer atmosphere. In that case, accurate CO_2 slant density values extend down to altitudes as low as 10 km.

[46] Figure 10 shows the vertical profile of the ozone slant density. As in the case of CO_2, ozone detection at low altitudes is limited by the amount of aerosol extinction. In the case shown in the figure, the atmosphere is opaque at 250 nm below 30 km.

[47] Figure 11 shows the corresponding optical thickness at 200 nm resulting from the column density of aerosols. The transmission is zero below 30 km, which means that the atmosphere transmits no starlight below that altitude. It is interesting to note that the local maximum at 40 km is the signature of a cloud or a detached layer of dust at that altitude [*Montmessin et al.*, 2006]. Above 60 km, absorption by aerosols becomes marginal and the values given there correspond to the noise in the transmission measurement.

[48] The next section shows how local densities are computed from the slant density profiles.

4. Vertical Inversion

[49] Local density profiles are derived from slant density profiles using a standard inversion algorithm called the onion peeling method which has been applied to various experiments. We assume that the atmosphere is spherically symmetric along the relevant lines of sight. Figure 12 shows the geometry for the vertical inversion.

[50] The relation between the slant density N and the local density $D(z)$ is given by an Abel integral,

$$N = \int_{-\infty}^{+\infty} D(s)ds = 2\int_{R_{mnp}}^{+\infty} D(z)\frac{z}{\sqrt{z^2 - R_{mnp}^2}}dz, \quad (4)$$

where s is an abscissa along the LOS, z the corresponding distance of the point to the center of Mars, and R_{mnp} the

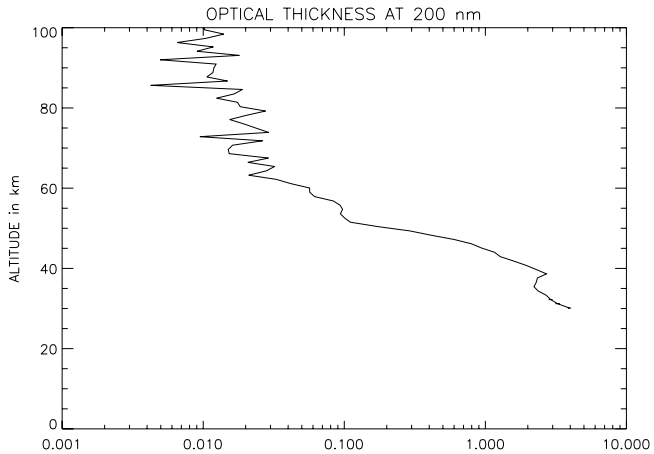

Figure 11. Dust optical thickness in the line of sight as a function of altitude of the point nearest to Mars. The optical thickness is computed for 200 nm. The cross section is proportional to $1/\lambda$. Below 30 km the atmosphere is opaque and the optical thickness cannot be determined. The local maximum at 40 km shows the presence of a cloud or a detached layer of dust. Negative values above 80 km are eliminated in this logarithmic scale plot. The noise is about 0.01–0.02; i.e., there is no absorption measured above 60 km.

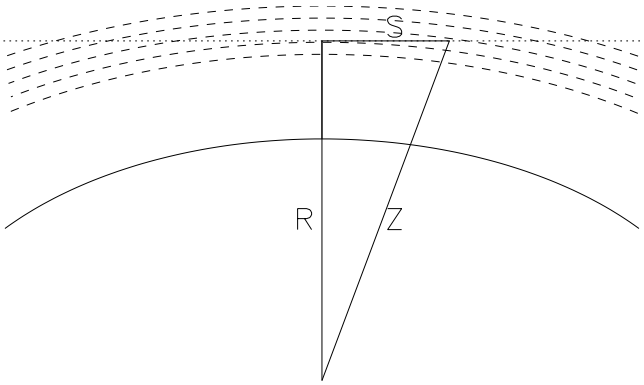

Figure 12. The geometry of the inversion. R is the distance from the center of Mars to the nearest point of the line of sight *MNP*. Z is the distance from the center of Mars to the layer. The altitude of the layer is obtained by subtracting the radius of Mars at the point of inversion, as defined by an ellipsoid about an equipotential.

distance of the Mars Nearest Point of the LOS to the center of Mars.

[51] The previous relation between the observed slant densities N and the local densities D can be written as follows

$$\mathbf{N} = [\mathbf{A}] \cdot \mathbf{D} + \varepsilon. \tag{5}$$

N is a vector containing the slant density values obtained from the spectral inversion. **D** is a vector containing the local density values on a given grid. The matrix [**A**] expresses the relation between the local density vector and the slant density vector. **N** and **D** are defined for the same altitudes. This means that matrix [**A**] is square in our algorithm. The vector ε describes the statistical error associated with the values **N**. The coefficients A_{ij} of the matrix are deduced from the relation above by

$$A_{ij} = 2 \int_{z\min_j}^{z\max_j} f(z) \frac{z}{\sqrt{z^2 - R_i^2}} dz. \tag{6}$$

The values $z\min_j$ and $z\max_j$ give the limits of integration for layer j. The function $f(z)$ gives the variation of local density in the layer. It can be a linearly interpolated function between node values. R_i is the Mars Nearest Distance for the line of sight of data N_i.

[52] The covariance matrix [$\mathbf{C_N}$] or error matrix associated with the slant density vector is a diagonal matrix. Its ith element is equal to the square of the statistical error associated with the slant density N_i derived from the spectral inversion. This problem has been widely studied because of the extensive data obtained by stellar occultations in the atmosphere of Earth, in particular in connection with the GOMOS experiment.

[53] An estimator of the local density $\widehat{\mathbf{D}}_0$ is obtained by

$$\widehat{\mathbf{D}}_0 = [\mathbf{K_0}] \cdot \mathbf{N}, \tag{7}$$

where the matrix [$\mathbf{K}_0$] satisfies the following relation

$$[\mathbf{K_0}] = \left([\mathbf{A}]^T [\mathbf{C_N}]^{-1} [\mathbf{A}]\right)^{-1} \cdot \left([\mathbf{A}]^T [\mathbf{C_N}]^{-1}\right). \tag{8}$$

The covariance matrix associated with this estimator is given by

$$\begin{aligned} [\mathbf{C_{D_o}}] &= [\mathbf{K_0}] \cdot [\mathbf{C_N}] \cdot [\mathbf{K_0}]^T \\ &= \left([\mathbf{A}]^T [\mathbf{C_N}]^{-1} [\mathbf{A}]\right)^{-1}. \end{aligned} \tag{9}$$

In most cases, the results obtained using this relation show an amplification of the noise in the slant density data. To decrease this effect, we use a classical method called the Tikhonov regularization method [*Tikhonov and Arsenin*, 1977; *Twomey*, 1977]. The idea is to introduce a smoothness constraint which will decrease the effect of the noise in the derived profile. Following this method, the solution becomes

$$\begin{aligned} [\mathbf{K}] = &\left([\mathbf{A}]^T [\mathbf{C_N}]^{-1} [\mathbf{A}] + \lambda_s [\mathbf{L}]^T [\mathbf{L}]\right)^{-1} \\ &\cdot \left([\mathbf{A}]^T [\mathbf{C_N}]^{-1}\right). \end{aligned} \tag{10}$$

[54] The matrix [**L**] is defined below. It corresponds to the second derivative operator, where h is the distance between two consecutive layers.

$$[\mathbf{L}] = \frac{1}{h^2} \begin{vmatrix} -1 & 1 & 0 & 0 & \dots & 0 \\ 1 & -2 & 1 & 0 & \dots & 0 \\ 0 & 1 & -2 & 1 & \dots & 0 \\ \dots & \dots & \dots & \dots & \dots & \dots \\ 0 & \dots & 0 & 1 & -2 & 1 \\ 0 & \dots & 0 & 0 & 1 & -1 \end{vmatrix}.$$

[55] The smoothness constraint is characterized by the coefficient λ_s. A large value of this coefficient gives more weight to the regularization constraint which means that more layers are used to derive the local density, resulting in a degradation of the vertical resolution.

[56] Following *Rodgers* [2000], we introduce the averaging kernel as the matrix that expresses the relation between the result of the inversion scheme $\widehat{\mathbf{D}}$ (the estimator) and the actual density profile. Using equations (2) and (4),

$$\widehat{\mathbf{D}} = [\mathbf{K}] \cdot \mathbf{N} = \underbrace{[\mathbf{K}] \cdot [\mathbf{A}]} \cdot \mathbf{D} + [\mathbf{K}] \cdot \varepsilon. \tag{11}$$

The i^{th} line of the averaging kernel shows the influence during the inversion of all the layers on the i^{th} density value. Figure 13 gives examples of the lines of the averaging kernel. First we see that this function is peaked at the diagonal value, meaning that the estimator is close to the actual density. The strong oscillation between positive and negative values is a remainder of the Abel integral inversion ($\lambda_s = 0$). We see also that the influence is not symmetric around the considered layer because line of sight integration includes layers above the tangent altitude but not below. Finally, increasing the value of the regularization parameter λ_s increases the relative value of the secondary terms. This means that the estimated value is a weighted average of

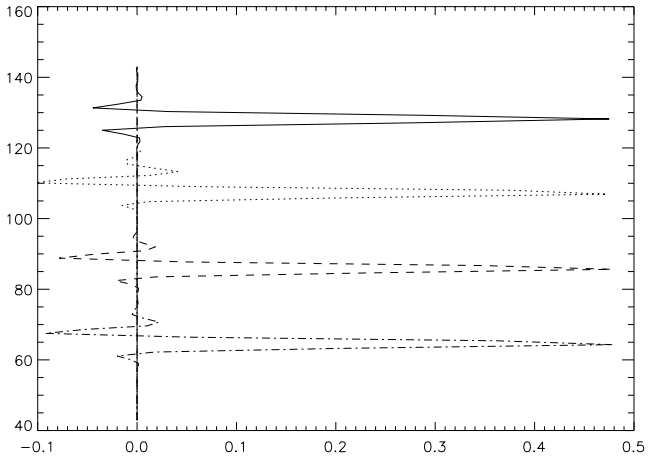

Figure 13. Lines of averaging kernels for various layers. The abscissa shows the coefficient of the averaging kernel, and the ordinate shows the altitude in kilometers. Each distribution is disymmetric with a larger influence for the layers above the considered layer.

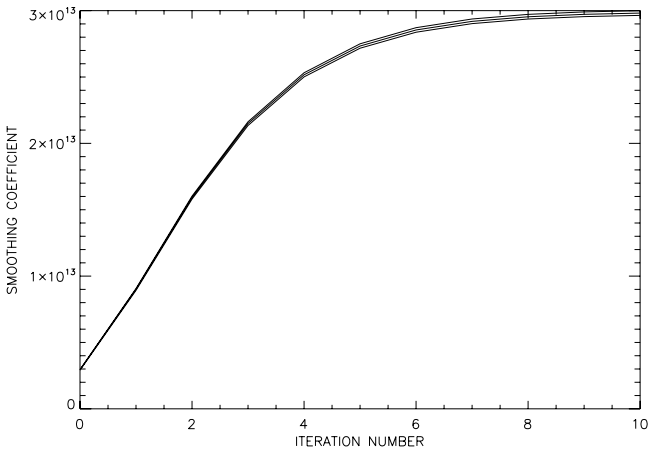

Figure 14. Smoothing coefficient λ_s values for 10 iterations. The coefficient is shown at three different altitudes around 50, 80, and 110 km. λ_s values are very similar due to the normalization scheme in equation (10).

more layers as λ_s increases, thus degrading the vertical resolution of the derived profile.

[57] Various authors [*Rodgers*, 2000] have used the Backus-Gilbert spread $s(z)$ to evaluate the vertical resolution. This quantity for altitude z is defined by

$$s(z) = 12\,\frac{\int_0^\infty (z-u)^2 A_z(u)^2 du}{\left(\int_0^\infty A_z(u) du\right)^2}, \qquad (12)$$

where A_z is the averaging kernel for altitude z (Figure 13).

[58] Choosing the correct regularization parameter can be difficult. On one hand, low values of λ_s give poor regularization and a noisy density profile; on the other hand high values of λ_s give smooth profiles with degraded vertical resolution. Choosing the right value of λ_s is a trade-off between those two aspects of the retrieved profile.

[59] The algorithm used here has been developed by Hauchecorne and Cot (private communication). First we must note that the regularization parameter does not have to be constant with altitude. The amount of smoothing required is not the same everywhere on the profile. The best results have been obtained by choosing a value of $\lambda_s(z)$ proportional to $1/\sigma_D(z)^2$ where $\sigma_D(z)$ is the error in the estimated density at altitude z. To compute the value of λ we apply the following scheme.

[60] First, we do an initial Abel inversion with no regularization. This yields a noisy profile. Statistical errors of the derived profile are computed using equation (6). The corresponding $\lambda_s(z) = \lambda_0/\sigma_D(z)^2$ is then applied to the next iteration and new error estimates are computed. This scheme is iterated until the error does not change, showing that an optimum has been reached. The variation of the coefficient is shown in Figure 14. In most cases, convergence is obtained in a few iterations and after 10 iterations $\lambda_s(z)$ is always stable for all altitudes.

[61] The typical vertical resolution of the profiles (equation (9)) obtained using this algorithm varies between 3 to 10 km, the latter value obtained in the most noisy cases.

[62] An alternate solution has been suggested [*Tamminen et al.*, 1998]. In that case, the vertical resolution is fixed to a predetermined value and λ_s is then chosen to achieve this vertical resolution. This means that the statistical error on the retrieved density is not optimal.

[63] Figure 15 shows the local density profile after inversion of the slant density profile shown in Figure 10.

[64] Either one of these schemes can be used to invert the slant density profiles. Obviously here, a trade-off is necessary between vertical resolution and statistical error. In this work we have not been able to identify a best solution for the value of the smoothing coefficient and we have chosen

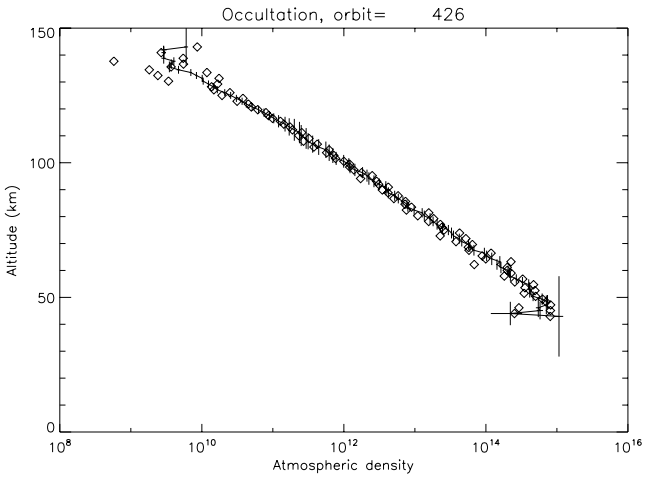

Figure 15. Carbon dioxide density profile after vertical inversion. Data are shown in cm^{-3} (x axis). This profile was obtained between 30 and 150 km from the slant density profile shown in Figure 9. The diamonds show the values obtained with $\lambda_s = 0$ (no smoothness constraint). The thick line shows the result for an inversion with regularization as explained in the text. The barely visible horizontal lines show the error derived from the diagonal of the covariance matrix. The vertical lines show the Backus-Gilbert spread, i.e., the vertical resolution implied by the regularization scheme.

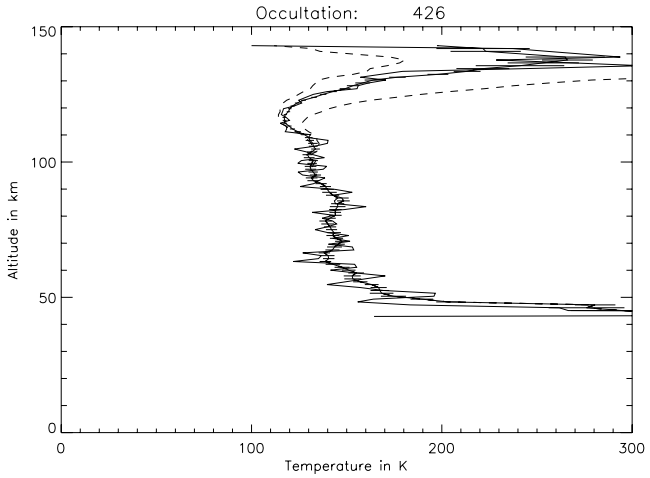

Figure 16. Temperature profile obtained from the density profile shown in the previous figure, assuming hydrostatic equilibrium between the layers. The thin line shows the raw result. The thick line shows a sliding average over 3 km corresponding to the vertical resolution of the density profile. As mentioned in the text, the temperature is assumed to be 150 K at 150 km. To evaluate the effect of this assumption, we have added two dashed lines corresponding to a temperature at 150 km of 50 K and 300 K. All profiles give identical values below 110 km.

an iterative scheme which gives a solution that is not unique.

5. Temperature Profiles

[65] Temperature profiles are derived following the method described by *Hauchecorne and Chanin* [1980] and *Korablev et al.* [2001]. The pressure is derived from the density profile computed from the vertical inversion. Using hydrostatic equilibrium, we have

$$dP(z) = -\rho(z)\, g(z)\, dz, \tag{13}$$

where the pressure P and local density ρ are functions of altitude z. The local gravity $g(z)$ varies with altitude. If the gravity value is g_o at the surface of Mars and r_o is the radius of the planet, we have $g(z) = g_o \frac{r_o^2}{(r_o+z)^2}$. Then we find

$$P(z) = P(z_{\max}) + \int_z^{z_{\max}} \rho(u)\, g_o\, \frac{r_o^2}{(r_o+u)^2}\, du. \tag{14}$$

Assuming a temperature at altitude $z_{\max}$,

$$T(z) = \frac{P(z)}{n(z)\,k} = \frac{T(z_{\max})\, n(z_{\max})}{n(z)} + \frac{1}{n(z)\,k}\left(\int_z^{z_{\max}} n(u)\, g_o\, \frac{r_o^2}{(r_o+u)^2}\, du\right). \tag{15}$$

[66] Figure 16 shows the temperature profile obtained using expression (12). The errors are derived from the propagation of the errors for the density profile. The temperature at 150 km is assumed to be 150 K. As seen in Figure 16, the effects of this assumption become negligible below 110 km. Of course, the vertical resolution used to characterize the regularization constraint for the density profile also applies to the temperature profile.

[67] Below 50 km, the profile clearly gives unreliable results due to the noise in the density profile. This is a typical case in the SPICAM occultation data, although some profiles with low aerosol content at lower altitudes can extend down to 20 km.

6. Conclusion

[68] In this paper we have detailed the various steps of the algorithm that we use for processing the SPICAM stellar occultation data.

[69] We have shown how we can derive CO_2, O_3 and aerosol column densities below 150 km. This step is called spectral inversion. It relies upon a good knowledge of the absorption cross section of the species that we wish to estimate. At the present point in our processing, we assume that the cross sections are independent of temperature and we use empirical values obtained for temperatures close to 200 K.

[70] The second step of the processing is called vertical inversion. It is based on the onion peeling method and allows computing local density profiles from slant density profiles, assuming that the atmosphere is locally spherically symmetric. We have shown that the inversion of the Abel integral alone leads to an amplification of the noise of the slant density profile.

[71] It is then necessary to use a Tikhonov regularization constraint to obtain a smoother solution. This method relies on the use of an altitude dependent regularization parameter which is iteratively defined by a minimization of the local density error. The use of the regularization term creates a correlation between the different layers and can be seen as a degradation of the vertical resolution. The new vertical resolution, typically between 3 and 6 km, is estimated from the Backus-Gilbert spread [*Rodgers*, 2000].

[72] Finally we show that accurate temperature profiles can be obtained below 110 km from the vertical profiles of density. Below 50 km, profiles are very uncertain due to the preponderance of aerosol extinction. It must be noted here that SPICAM solar occultations give better results at lower altitudes. This will be presented in a future work.

[73] Future work based on these data will try to evaluate the effects of the possible variations of the CO_2 cross section with temperature. A preliminary look at the data shows that there may be a significant variation of the cross section below 135 nm. This spectral region shows an unsaturated absorption above 100 km, where the actual temperature is well below the assumed value of 195 K. We will need to evaluate the effect this may have on the derivation of slant densities, and then on local density profiles.

[74] Figure 17 shows the relative difference of cross section per Kelvin. For temperature well below 195 K, we may expect some non-negligible errors when using the cross section at 195 K. One problem is that the cross section was measured by *Yoshino et al.* [1996] only at 195 and 295 K, while we would need at least the temperature gradient around 195 K, a temperature more relevant to the atmosphere of Mars. There is however a wavelength region around 140 nm where the cross section is most likely insensitive to temperature. One can therefore determine the slant densities only from this particular region, invert

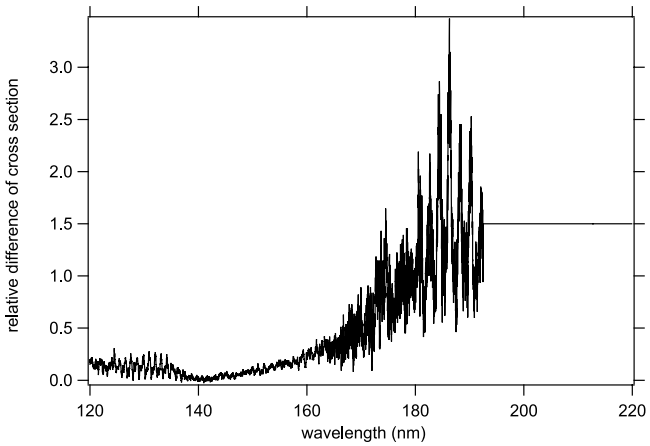

Figure 17. CO_2 absorption cross-section measurements by *Yoshino et al.* [1996] were made at 195 and 295 K. The difference of cross section between 195 and 295 K (relative to cross section at 195) is plotted. Note that the cross section is almost insensitive to temperature around 140 nm.

the vertical distribution, and determine the temperature profile (see next section). Then, one could use the atmosphere of Mars itself as a gigantic absorption cell to determine the CO_2 cross section at temperatures other than 195 K, in particular below 195 K. Possibly this could work better by averaging several occultations together to improve the accuracy of such an exercise.

[75] Another effect might also be of some importance. We have used a forward transmission model with a cross section averaged over 1.5 nm to match the SPICAM spectral resolution, and to save computing time in the fitting process. However, the transmission computed with an averaged cross section is different from the average of the transmission computed at high spectral resolution, because of the highly structured pattern of the cross section wavelength dependence. The difference may amount to 2–3% for values of the CO_2 slant densities around 3×10^{18} mol.cm^{-2}, but in a limited wavelength range (125–135 nm). Since we use a much larger interval to fit the transmission, the error on the slant density made by using the averaged cross section should be smaller than 2–3%.

[76] Finally, the processing algorithm described here will be applied to all SPICAM occultation data to create a database of carbon dioxide and ozone density profiles and also dust/aerosols profiles [*Montmessin et al.*, 2006]. This will be the basis of various analyses of the SPICAM data to better constrain the global circulation models of Mars and to study the photochemistry processes in the Martian atmosphere.

[77] **Acknowledgments.** Mars Express is a space mission from ESA (European Space Agency). We express our gratitude to all ESA members who participated in this successful mission. We also thank Astrium for the design and construction of the spacecraft. We thank our collaborators at the three institutes for the design and fabrication of the instrument (Service d'Astronomie/France, BIRA/Belgium, and IKI/Moscow). We thank CNRS and CNES for financing SPICAM in France. We thank the Space Division of the Belgian Federal Science Policy Office for supporting this project through the ESA PRODEX program. The Russian team acknowledges support of RFFI grant 04-02-16856-a. We thank NASA for support of our American collaborators.

References

Bertaux, J.-L. (2006), Introduction to the special section: SPICAM on Mars Express, *J. Geophys. Res.*, doi:10.1029/2006JE002760, in press.

Bertaux, J.-L., et al. (2005), Nightglow in the upper atmosphere of Mars and implications for atmospheric transport, *Science*, *307*(5709), 566–569.

Esposito, L. W., C. A. Barth, J. E. Colwell, G. M. Lawrence, W. E. McClintock, A. I. F. Stewart, H. U. Keller, A. Korth, H. Lauche, and M. Festou (2005), The Cassini Ultraviolet Imaging Spectrograph Investigation, *Space Sci. Rev.*, *115*(1–4), 299–361.

Evans, W. F. J., H. C. Wood, and E. J. Llewellyn (1970), Ground-based photometric observations of the 1.27 μ band of O_2 in the twilight airglow, *Planet. Space Sci.*, *18*, 1065.

Festou, M. C., S. K. Atreya, T. M. Donahue, B. R. Sandel, D. E. Shemansky, and A. L. Broadfoot (1981), Composition and thermal profiles of the Jovian upper atmosphere determined by the Voyager ultraviolet stellar occultation experiment, *J. Geophys. Res.*, *86*, 5715–5725.

Hauchecorne, A., and M.-L. Chanin (1980), Density and temperature profiles obtained by lidar between 35 and 70 km, *Geophys. Res. Lett.*, *7*(8), 565–568.

Hays, P. B., and R. G. Roble (1968), Stellar spectra and atmospheric composition, *J. Atmos. Sci.*, *25*, 141.

Hays, P. B., and R. G. Roble (1973), Observation of mesospheric ozone at low latitudes, *Planet. Space Sci.*, *21*(2), 273–279.

Hays, P. B., R. G. Roble, and A. N. Shah (1972), Terrestrial atmospheric composition from stellar occultations, *Science*, *176*(4036), 793–794.

Korablev, O., J. L. Bertaux, and J. P. Dubois (2001), Occultation of stars in the UV: Study of the atmosphere of Mars, *J. Geophys. Res.*, *106*(E4), 7597–7610.

Lebonnois, S., E. Quémerais, F. Montmessin, F. Lefèvre, S. Perrier, J.-L. Bertaux, and F. Forget (2006), Vertical distribution of ozone on Mars as measured by SPICAM/Mars Express using stellar occultations, *J. Geophys. Res.*, doi:10.1029/2005JE002643, in press.

Montmessin, F., E. Quémerais, J. L. Bertaux, O. Korablev, P. Rannou, and S. Lebonnois (2006), Stellar occultations at UV wavelengths by the SPICAM instrument: Retrieval and analysis of Martian haze profiles, *J. Geophys. Res.*, doi:10.1029/2005JE002662, in press.

Press, W. H., S. A. Teukolsky, W. T. Vetterling, and B. P. Flannery (1986), *Numerical Recipes in Fortran*, Cambridge Univ. Press, New York.

Riegler, G. R., S.-C. Liu, R. J. Cicerone, and J. F. Drake (1976), Stellar occultation measurements of atmospheric ozone and chlorine from OAO-3, *J. Geophys. Res.*, *81*, 4997–5001.

Riegler, G. R., S. C. Liu, B. Wasser, S. K. Atreya, T. M. Donahue, and J. F. Drake (1977), UV stellar occultation measurements of night time equatorial ozone, *Geophys. Res. Lett.*, *4*, 145–148.

Rodgers, C. D. (2000), *Inverse Methods for Atmospheric Sounding*, 238 pp., World Sci., Hackensack, N. J.

Sandel, B. R., and A. L. Broadfoot (1986), Statistical performance of the intensified CCD, *Appl. Opt.*, *25*, 4135.

Smith, G. R., and D. M. Hunten (1990), Study of planetary atmospheres by absorptive occultations, *Rev. Geophys.*, *28*, 117–143.

Tamminen, J., H. Haario, E. Kyrola, L. Oikarinen, and E. Saksman (1998), Data processing of the GOMOS instrument by using an adaptive MCMC method, in *Earth Observing Systems III*, edited by W. L. Barnes, *Proc. SPIE Int. Soc. Opt. Eng.*, *3439*, 470–479.

Tikhonov, A. N., and V. Y. Arsenin (1977), *Solutions of Ill-Posed Problems*, V. H. Winston, Washington, D. C.

Twomey, S. (1977), Some aspects of the inversion problem in remote sensing, in *Inversion Methods in Atmospheric Remote Sounding*, pp. 41–65, NASA Langley Res. Cent., Hampton, Va.

Yee, J., et al. (2002), Atmospheric remote sensing using a combined extinctive and refractive stellar occultation technique: 1. Overview and proof-of-concept observations, *J. Geophys. Res.*, *107*(D14), 4213, doi:10.1029/2001JD000794.

Yoshino, K., J. R. Esmond, Y. Sun, W. H. Parkinson, K. Ito, and T. Matsui (1996), Absorption cross section measurements of carbon dioxide in the wavelength region 118.7–175.5 nm and the temperature dependence, *J. Quant. Spectrsc. Radiat. Transfer*, *55*(1), 53–60.

J.-L. Bertaux, C. Cot, E. Dimarellis, and E. Quémerais, Service d'Aéronomie, BP3, F-91371 Verrières le Buisson, France. (eric.quemerais@aerov.jussieu.fr)

D. Fussen, Institut d'Aéronomie Spatiale, 3 Avenue Circulaire, B-1180 Bruxelles, Belgique.

O. Korablev, Space Research Institute (IKI), 84/32 Profsoyuznaya, 117810 Moscow, Russia.

B. R. Sandel, Lunar and Planetary Laboratory, 1629 East University Boulevard, Tucson, AZ 85721-0092, USA.